Minerals Engineering 26 (2012) 5–12

Contents lists available at SciVerse ScienceDirect

Minerals Engineering

journal homepage: www.elsevier.com/locate/mineng

Flotation process fault detection using output PDF of bubble size distribution ☆

Canhui Xu, Weihua Gui, Chunhua Yang *, Hongqiu Zhu, Yiqiu Lin, Cao Shi

School of Information Science and Engineering, Central South University, Hunan 410083, China

ARTICLE INFO

Article history:
Received 26 April 2011
Accepted 20 September 2011
Available online 25 November 2011

Keywords:
Froth flotation
Film size
Bubble size
Output PDF
Fault detection

ABSTRACT

As an important indicator of flotation performance, bubble structure is believed to be related with the addition amount of chemical reagent. To differentiate film size calculated from surface froth image segmentation and underlying bubble size, post-segmentation analysis is carried out to archive the prediction of bubble size distribution from the known bubble film distribution. Based on the facts that the probability density distribution (PDF) of film size is found to be non-Gaussian and singular feature characterizing bubble structure becomes insufficient, a nonparametric kernel estimator is introduced to approximate the output PDF of bubble size distribution. Through transforming nonparametric description into dynamic kernel weight vectors, an output PDF based detection filter is designed, according to which LMIs are established to solve its stability condition by Lyapunov stability analysis on the estimated error system. Fault detection problem is then solved through a threshold criterion determined by the system stability condition. Simulation results show that desired fault detection for reagent addition in industrial froth flotation can be achieved using the proposed method.

© 2011 Elsevier Ltd. All rights reserved.

1. Introduction

Froth flotation is a complex physical and chemical process influenced by multiple operational variables such as inlet air flow, froth depth and reagent addition. It is well recognized that froth visual appearance observed can characterize the combining effect of multiple process conditions on flotation, and it is also known as the indicator of flotation separation performance (Moolman et al., 1996a). Recent advances in image processing and computer vision based froth appearance monitoring systems contribute greatly to the feature extraction of visual descriptors. An elaborate summary of existed physical and dynamic froth features extraction was reported (Aldrich et al., 2010), and it is pointed out linking the measurable visual froth attributes and flotation performance remains challenging and demands continuous research.

As one of the dominant visual features, bubble size has attracted great interest from both academic and industrial researchers. Although the advent of X-ray tomography devices has given various insights on two phase foams, the inherent opaque property of industrial froth limits their application on bubble structure description (Monnereau and Vignes-Adler, 1998). Computer-aided images processing becomes a reasonable solution to interpret the froth appearance automatically due to its simplicity and low cost (Aldrich et al., 1997). From then, froth segmentation techniques are discussed for subsequent bubble size feature extraction. Numerous computer vision based approaches have been reported to segment the closely packed surface bubbles including white spots detection (Wang and Wang, 2000), watershed method (Bonifazi et al., 2001; Sadr-Kazemi and Cilliers, 1997), wavelet transformation (Liu and MacGregor, 2008; Liu et al., 2005), valley edge detection (Wang et al., 2003) and their varieties (Yang et al., 2009b). However, post-segmentation analysis is confined to extract singular feature such as average surface film size or variance for analysis convenience, with the unreliable assumption that the surface film size distribution is Gaussian. There also exists several attempts of classifying bubble size into several categories such as large, middle and small size (Holtham and Nguyen, 2002; Liu et al., 2005), to each of which corresponding operating strategy set can be performed. A more recent simulation research emphasizes the remarkable difference between the surface film size distribution and the surface bubble size distribution (Wang and Neethling, 2006), which indicates that more often computer vision based research on bubble structure tends to simply regard the surface film size calculated from froth image segmentation as the actual bubble size. Wang proposed an empirical formula that relates the surface film size distribution and the internal bubble size distribution (Wang and Neethling, 2009). It is worth noticing that the probability density distribution (PDF) of surface film size is found to be non-Gaussian (Yang et al., 2009a). Further exploring of the information indicated by froth structure has shown that the film size distribution is highly skewed, which neither belongs to any existing mathematical model based distribution. To depict

☆ Grant sponsors: This article is supported by the Fundamental Research Funds for the Central Universities under Grant No. 2011JQ009 and Key Program by National Natural Science Foundation of China No. 61134006.

* Corresponding author. Tel.: +8613975894870.
E-mail address: ychh@mail.csu.edu.cn (C. Yang).

0892-6875/$ - see front matter © 2011 Elsevier Ltd. All rights reserved.
doi:10.1016/j.mineng.2011.09.012

Nomenclature

h_{Hist}	unbiased optimal bin width of the histograms
n_b	number of surface films provided by the segmented froth image
r_f	radius of the 2D surface film
r_b	radius of the 3D bubble
$f\left(\frac{r_f}{r_b}\right)$	frequency distribution of r_f/r_b
$S(r_b)$	frequency distribution of bubble size
$F(r_f)$	frequency distribution of film size
$f(x)$	probability density function
$K(x)$	pre-specified kernel function
w_i	weight of the ith kernel function
h	window width of the kernel estimation
Z_i	center point of the ith kernel function along the horizontal axis
$f_{\ker}(z, u)$	output PDF
$u(t)$	control input
$\omega(z, u, F)$	approximation error
$\hat{x}(t)$	estimation of the state $x(t)$
A, A_d, H, H_d, E	identified system parameter matrices of the weight system
d	positive constant representing the time delay
L	filter gain
σ	standard deviation of the surface film size population
$\varepsilon(t)$	residual signal
$\sigma(z)$	pre-specified weight vector
β	threshold of the system
δ	supremum of approximation error

the unknown continuous process of froth flotation, nonparametric estimation provides a credible solution. Commonly used nonparametric estimation techniques include histogram, frequency polygon, shift average histogram, kernel methods, wavelet method, and B-spline expansion models (Zhang et al., 2006). Theoretical researches on tracking the output PDFs to a target distribution shape by using various control approaches (Guo et al., 2008) can also increase the possibility of froth visual features based process control.

To relate the flotation operation condition with bubble structure, O'Connor et al. revealed that the increase in pH causes bubble size to increase (O'Connor et al., 1990). Consequently, the variance of bubble size has great effect on the probability of collision between mineral particles and bubbles, as well as the adhesion of these particles to the bubbles. According to the principle that the length of Plateau border per unit volume of foam is reversely proportional with the square of the radius of individual bubble sphere and meanwhile positively proportional to process water recovery, the continuous increase of bubble size can lead to lower total surface area with decreased water recovery and result in the deteriorating performance of mineral concentration flow rate as well as mineral recovery. Moolman also claimed that the result is consistent with the observation in the case of pyrite, and the mineral recovery decreased at higher pH's (Moolman et al., 1996b). Conventionally, industry process fault detection heavily depends on the frequent inspection of froth views and manipulation of experienced human operators, which is often problematic with serious delayed responses. Along with the implementation of online monitoring system of froth visual appearance, quantitative fault detection becomes highly desired and essential to maintain the operational variables at acceptable rates. Cilliers proposed a quantitative fault detection and diagnosis model which is successfully applied for hydrocyclones (Cilliers and Swartz, 1995). In industrial case studies of apatite and sphalerite flotation, it is revealed that the overall mineral concentration changes were essentially caused by the chemical addition, accompanied by clearly froth spectral intensity changes, on basis of which a fault detection scheme is introduced (Niemi et al., 1997).

This work aims to explore the froth structure by using kernel density estimation technique to approximate the output PDF of surface bubble size distribution rectified by the empirical formula and its application on process fault detection. Nonparametric kernel descriptor is designed to reflect the variety of the PDF curve such that the output PDF is formulated in terms of dynamic weights, by which a system model with time delay is established. And an effective fault detection criterion is determined by using linear matrix inequation method. The chemical reagent addition fault is successfully detected on the industrial data of off-line froth images. Next section introduces bubble characteristic oriented watershed segmentation scheme and post-segmentation analysis. Section 3 presents the nonparametric density estimation and kernel density estimators. The kernel weight vector based fault detection filter model is proposed in Section 4. Section 5 presents the experimental results and discussion. Conclusion is provided in the last section.

2. Surface 2D film size distribution to 3D bubble size distribution

Experimental setup consists of RGB camera with resolution of 600×800 and lens of 49 mm, high frequency light source, cover hook protecting camera from dust and ambient light, optical fiber with length over 200 m for signal communication to industrial PC computer in operating room, shown in Fig. 1. The camera is mounted 110 cm vertically above the froth surface of the target cell, and froth images with window size 12×9 cm^2 are captured online at the rate of 7.5 frames/s. Meanwhile, the corresponding process operational and performance data are collected on industrial scale.

Froth images collected from industry field displays that each bubble has a convex shape which leads to the appearance of white spots. The existing froth segmentation methods such as white spot

Fig. 1. Image acquisition hardware configuration. Image acquisition hardware configuration in flotation industry includes: RGB camera with resolution of 600×800, high frequency light source, cover hook protecting camera from dust and ambient light, optical fiber with length over 200 m for signal communication to industrial PC computer in operating room. The camera is mounted 110 cm vertically above the froth surface of the target cell, and froth images with window size 12×9 cm^2 are captured online at the rate of 7.5 frames/s.

detection, watershed, and valley edge detection are derived from this fact. Froth image observed is a type of gradient images. The highest gradient with high grayscale values often appears to be around white spots, which are not the target boundaries between bubbles. The real edges between bubbles are with lower gradient magnitude, some of which are local minimum intensity. Watershed based segmentation happens to be able to detect the catchment basins of all minima marked beforehand, which provides a solution to segment bubbles without background region. To find the accurate watershed lines separating bubbles, morphological opening and closing based reconstruction using iterated gray-scale dilations is firstly applied for de-noising purpose. The white spotlights reflected on each bubble are extracted as makers. The watershed line can be eventually identified through the accomplishment of immersion process. Segmentation result of the on-line acquired froth image in rougher cell is shown in Fig. 2.

It is admitted that the bubble structure is of great importance. Neethling claims that bubble size determines water recovery with an inverse squared relationship (Neethling et al., 2003). Recently, bubble size is used as factor in a simplified froth recovery model. Ross points out that using only average bubble size as bubble structure feature can cause misleading or even false conclusion (Ross, 1991). Nevertheless, researchers tend to only focus on extracting singular statistical features such as mean, standard deviation, kurtosis or skewness representing the bubble structure, which are incapable of representing the entire profile of bubble size probability density distribution. Another misleading point is the shortage of understanding on the difference between the surface film size distribution and the surface bubble size distribution. Computer vision based research on bubble structure tends to simply regard the surface film size calculated from froth image segmentation as the actual bubble size.

To solve above two problems, the empirical formula proposed by Wang and Neethling (2009) is used to relate the surface film size distribution and the internal bubble size distribution. After segmenting the bubble films, the surface film size distribution is provided using histogram estimation. The unbiased optimal bin width h_{Hist} of the histograms (Scott, 1979) is determined by:

$$h_{Hist} = \left(\frac{24\sigma^3\sqrt{\pi}}{n_b}\right)^{1/3} \approx 3.5\sigma n_b^{-1/3} \tag{1}$$

where n_b is the number of samples which refers to the number of surface films provided by the segmented froth images, σ is the standard deviation of the surface film size population.

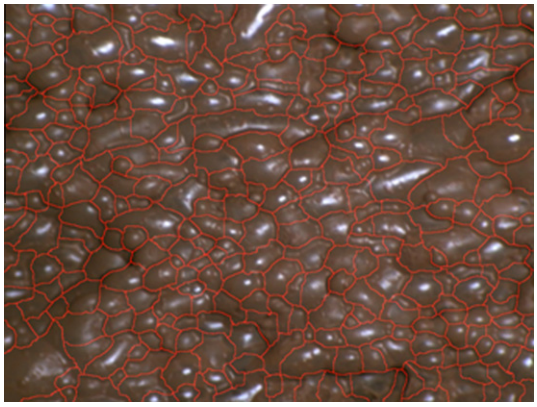

Fig. 2. Segmented froth image. Morphological opening and closing based reconstruction using iterated gray-scale dilations is applied for de-noising purpose. The spotlights reflected on each bubble are extracted as makers. The watershed line can be eventually identified through the accomplishment of immersion process. Segmentation result of the on-line acquired froth images in rougher cell is presented.

Film size is affected by the bubble radius, the distortion and the position of a bubble relative to its adjacent surface bubbles. Wang points out that there is no simple one-to-one relationship between film size and bubble size (Wang and Neethling, 2009). Observation from simulation has shown that the ratio of the 2D surface film size r_f to 3D bubble size r_b displays a frequency distribution independent of bubble dispersity level, which can be estimated by an empirical formula for constrained surfaces:

$$f\left(\frac{r_f}{r_b}\right) = \frac{3.51(r_f/r_b)^{4.67}}{1+\exp(56.43(r_f/r_b-1.08))} \tag{2}$$

where $f(r_f/r_b)$ is the frequency distribution of r_f/r_b. Formula (2) is the key to relate the film size distribution and bubble size distribution, which can be expressed as:

$$F(r_f) = \int_{r_b=0}^{\infty} f\left(\frac{r_f}{r_b}\right) S(r_b)\,dr_b \tag{3}$$

with discrete form:

$$F(r_{fi}) \approx \sum_{r_{bi=0}}^{r_{bMax}} f\left(\frac{r_{fi}}{r_{bi}}\right) S(r_{bi})\Delta r_{bi} \tag{4}$$

The frequency distribution of film size $F(r_f)$ can be calculated from frequency distribution of bubble size $S(r_b)$ and the frequency distribution $f(r_f/r_b)$. The inverse prediction model can reconstruct the 3D bubble size distribution from a given 2D surface film size distribution, which is highly desirable for froth flotation. With the given 2D surface film size distribution provided by image segmentation analysis, the successive aim is to predict the surface bubble size distribution based on the known film size distribution. By formula (4), numerical iteration updating $S(r_b)$ is used to recalculate the estimation values for $F(r_f)^*$ until the squared error $(F(r_f)^* - F(r_f))^2$ can be minimized and $S(r_b)$ remains positive for all r_b.

Fig. 3 shows the inverse prediction results. As expected, the difference between 2D film size distribution and 3D bubble size distribution are not remarkable due to its poly dispersity with NSD of 0.13 for segmented industrial froth image in Fig. 2. The size probability density distribution is found to be non-Gaussian with kurtosis value 4.94 and skewness value 0.85.

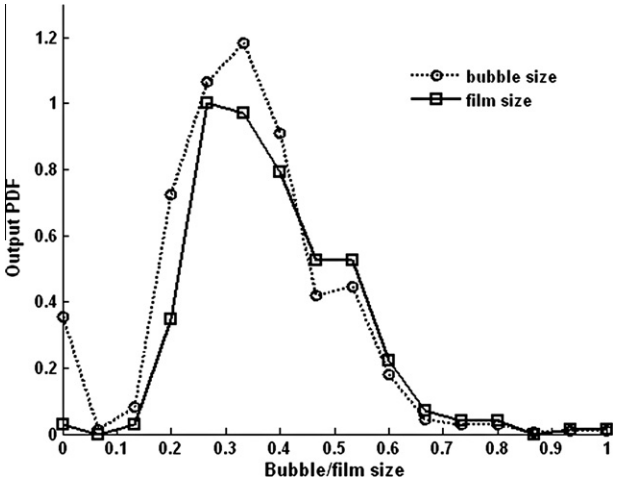

Fig. 3. Reconstructed 3D bubble size distribution from 2D surface film size distribution. The difference between 2D film size distribution and 3D bubble size distribution are not remarkable due to its poly dispersity with NSD of 0.13 for segmented industrial froth image.

3. Nonparametric kernel estimation

The post-segmentation analysis exhibits that probability density function (PDF) distribution of bubble size is non-Gaussian. Unlike traditional method applying singular feature such as mean or variance with the assumption that the distribution is normal, probability density distribution is suggested to accurately describe statistical feature of froth structure. The fact that the mathematical model of distribution is unknown makes nonparametric estimation method fitting to depict the unknown continuous process of froth flotation. Consider a probability density function $f(x)$ describing the probability distribution of x in (a,b):

$$P(a < x < b) = \int_a^b f(x)dx \tag{5}$$

Density estimation accomplishes the fitting of $f(x)$. Though classic nonparametric histogram estimator is good for data presentation, its discontinuity causes difficulty if derivatives of the estimates are required. A continuous version of the histogram is the frequency polygon formed by interpolating the midpoints of a histogram (Scott, 1985). Histogram based methods seek the balance between estimation accuracy and feature dimensionality, which can be very expensive for large samples. Apart from the histogram, the kernel estimator is most commonly used, which is given by:

$$\hat{f}_{Ker}(x) = \frac{1}{nh}\sum_{i=1}^{n} K\left(\frac{x - X_i}{h}\right) = \sum_{i=1}^{n} w_i K\left(\frac{x - X_i}{h}\right) \tag{6}$$

where the function $K(x)$ is the pre-specified kernel function satisfying $\int K(x)dt = 1$ to ensure a bona fide density estimate. w_i is the corresponding weight of the ith kernel function, and h is the window width. Based on the prototype of standard normal kernel function, a kernel function fitting for froth flotation is constructed as:

$$K\left(\frac{z - Z_i}{h}\right) = \frac{1}{h\sqrt{2\pi}} \exp\left(\frac{-\left(\frac{z-Z_i}{h}\right)^2}{2}\right) \quad -\infty < \frac{z - Z_i}{h} < \infty \tag{7}$$

where $K((z - Z_i)/h)$ is the ith kernel function, and Z_i is the center of the ith kernel function along the horizontal axis. Adjusting to the range of bubble radii, a number of kernel bases are selected to depict the size distribution. Its window width h is fixed across the entire sample. Fig. 4 illustrates 10 kernel bases with fixed window width, which is plotted in dashed line. Two dotted curves present the second and third kernel basis multiplying the corresponding weight coefficients. And the estimation result of Fig. 2 buzzle size distribution is plotted in solid line.

Fig. 5 presents the comparison of two density estimation methods of segmented froth image in Fig. 2. The optimal bin width of histograms is chosen based on formula (1). Comparison results have shown the kernel estimation can accomplish the description of bubble size probability density distribution with general lower feature dimensionality than histogram method.

4. Output PDF kernel estimation based fault detection

A fault is defined as the departure from an acceptable range of an observed output or operating variable (Himmelblau, 1978). Timeous detection of fault can determine whether the abnormal condition occurs (Cilliers and Swartz, 1995). In the case of froth description, it is reported that gradual increase of bubble size to certain degree can affect the critical pressure above which the bubbles rupture (Neethling and Cilliers, 2008) and will eventually lead to a fault condition deteriorating the process performance. The information indicated by bubble structure is a combining effect of multiple operational variables such as froth depth, inlet air flow and chemical reagents. It is known that by retaining the variance of froth depth and inlet air flow during a short period of time, bubble size is positively related to pH value which is determined by the dosage of activator Na_2Co_3. Human operators are in capable of performing timeous monitoring of various process variables, and the process manipulation mostly is relied on heuristics of their froth view observation. In some cases, the non-measurable input is to be inferred from the measured parameters, which requires a process model established so as to relate both sides (Isermann, 1984). By monitoring the froth appearance such as bubble size, the process fault status can be inferred and identified based on established system model.

Supposing there is a dynamic stochastic system with input $u(t) \in R^m$ and output $y(t) \in [a,b]$, the probability of output $y(t)$ lying in $[a,\xi)$ is defined as:

$$P(a \leqslant y(t) \leqslant \xi) = \int_a^{\xi} f_{\ker}(z,u)dx \tag{8}$$

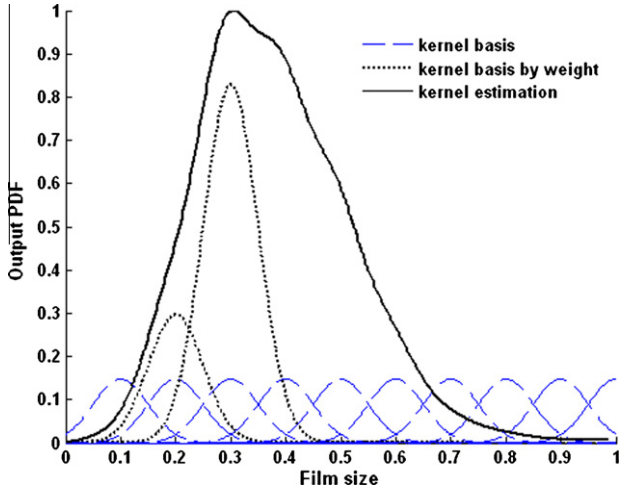

Fig. 4. Normal kernel estimation and the weight coefficients. Figure illustrates the choices of ten kernel bases with fixed window width, which is plotted in dashed line. Two dotted curve presents the second and third kernel basis multiplying the corresponding weight coefficients. The estimation result of Fig. 2 buzzle size distribution is plotted in solid line.

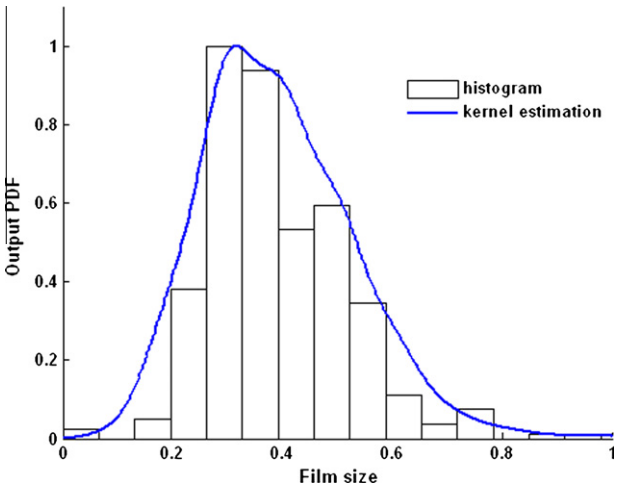

Fig. 5. Comparison between Normal kernel based method and histogram method for Fig. 2 bubble size density estimation. The optimal bin width of histograms is chosen based on formula (1). The comparison results show the kernel estimation can accomplish the description of probability density distribution of bubble size with lower feature dimensionality than histogram method.

where the $f_{ker}(z,u)$ represents the output PDF, in this case the PDF distribution of bubble size after froth image segmentation analysis. $u(t)$ is control input such as the input amount of Na_2CO_3 which is a dominant operational condition in the flotation system. The $f_{ker}(z,u)$ can be approximated by kernel estimators designed in formula (7) and the corresponding weights w_i.

To avoid the weight coefficients changing to negative values, the output PDF model with an approximation error $\omega(z,u,F)$ is adopted as follows:

$$\hat{f}_{ker}(z,u,F) = \sum_{i=1}^{n} w_i(u,F)K_i(z) + \omega(z,u,F) \tag{9}$$

where $K_i(z)$ $(i = 1,2,...,n)$ are pre-specified kernel function on $[a,b]$, $w_i(u)(i = 1,2,...,n)$ are the corresponding weight vector associated with $u(t)$. It can be supposed that $|\omega(z,u,F)| \leqslant \delta$, where δ is a known constant.

Denote

$$K_0(z) = [k_1(z), k_2(z), \ldots, k_{n-1}(z)]^T \tag{10}$$

$$W(t) = [w_1(u,F), w_2(u,F), \ldots, w_{n-1}(u,F)]^T \tag{11}$$

Since $\int_a^b \hat{f}_{ker}(z,u)dz = 1$, $\int_a^b k_i(z)dz = 1, i = 1,2\ldots\ldots n-1$, it is certain that there are $n-1$ independent weights. So (9) can be rewritten as:

$$\hat{f}_{ker}(z,u,F) = K^T(z)W(t) + h(W(t))k_n(z) + \omega(z,u,F) \tag{12}$$

where $K(z) = K_0(z)$, $h(W(t)) = 1 - \sum_{i=1}^{n-1} w_i(u,F)$, $h(W(t))$ is the corresponding weight of $k_n(z)$.

The description of the output buzzle size PDF has been transformed into a dynamic weight model, which is the key to design the fault detection filter. The following filter is designed as:

$$\begin{cases} \dot{\hat{x}}(t) = A\hat{x}(t) + A_d\hat{x}(t-d) + Hu(t) + H_du(t-d) + L\varepsilon(t) \\ \varepsilon(t) = \int_a^b \sigma(z)(f_{ker}(z,u(t),F) - \hat{f}_{ker}(z,u(t)))dz \\ W(t) = E\hat{x}(t) \end{cases} \tag{13}$$

where $\hat{x}(t)$ is the estimation of the state $x(t)$, A, A_d, H, H_d, E are the known system parameter matrices of the weight system, d is a positive constant representing the time delay, $L \in R^{m\times p}$ is the filter gain. Residual signal $\varepsilon(t)$ is formulated by the integral of the difference between the measured PDF and the estimated one. And $\sigma(z) \in R^{n\times 1}$ is a pre-specified weight vector on $[a,b]$. In practice, the residual signal $\varepsilon(t)$ can be regarded as the defined distance of the bubble size PDFs between two froth images before and after the fault.

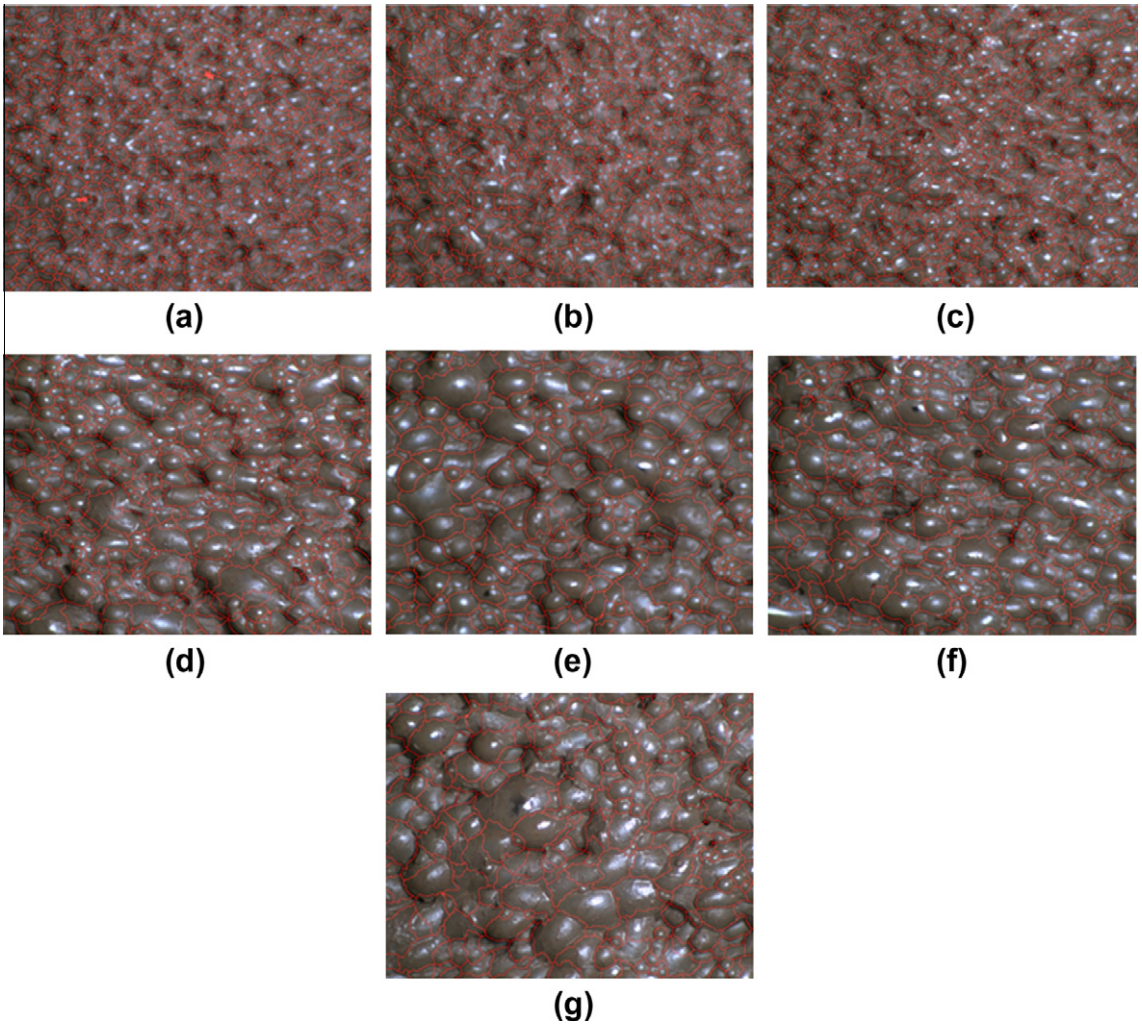

Fig. 6. Segmented industrial froth images captured on an hourly basis which are under the same condition in terms of resolution, angle, light condition, position, view scale, etc.

Define $\tilde{x}(t) = x(t) - \hat{x}(t)$ as the error state vector, which is used to describe the change of weight function before and after the output PDF curve changed. The estimated error system can be described as

$$\dot{\tilde{x}}(t) = (A - L\Gamma_1)\tilde{x}(t) + A_d\tilde{x}(t-d) - L\Gamma_2[h(Ex(t)) - h(E\hat{x}(t))] - L\Delta(t) \quad (14)$$

where $\Gamma_1 = \int_a^b \sigma(z)K^T(z)Edz$, $\Gamma_2 = \int_a^b \sigma(z)k_n(z)dz$, $\Delta(t) = \int_a^b \sigma(z)\omega(z,u,F)dz$.

According to the Lipschitz condition, there exists a known matrix U_1 satisfying:

$$\|h(Ex(t)) - h(E\hat{x}(t))\| \leqslant \|U_1E(x(t) - \hat{x}(t))\| \quad (15)$$

And the residual function can be acquired that

$$\varepsilon(t) = \Gamma_1\tilde{x}(t) + \Gamma_2(h(Ex(t)) - h(E\hat{x}(t))) + \Delta(t) \quad (16)$$

Since $|\omega(z,u,F)| \leqslant \delta$, it can be seen that $\|\Delta(t)\| = \|\int_a^b \sigma(z)\omega(z,u,F)\| \leqslant \tilde{\delta}$,

$$\tilde{\delta} = \delta\int_a^b \sigma(z)dz \quad (17)$$

Through using the output PDF based detection filter, a criterion can be designed to detect the fault. Lyapunov stability analysis is carried out on the estimated error system, and LMIs are established to solve its stability condition.

Theorem 1. For the parameter λ, if there exist matrices $P > 0$, $Q > 0$, R and constant $\eta > 0$ satisfying

$$\Psi = \begin{bmatrix} \Pi_0 + \eta I & PA_d & -\lambda R\Gamma_2 \\ A_d^T P & -I + \eta I & 0 \\ -\lambda\Gamma_2^T R^T & 0 & -I \end{bmatrix} < 0 \quad (18)$$

where $\Pi_0 = (PA - R\Gamma_1) + (PA - R\Gamma_1)^T + Q - \frac{1}{\lambda^2}E^TU_1^TU_1E$. Then the system is stable.

The proof of Theorem 1 is presented in Appendix A.

It is known from the proof that when system is stable, the error state vector satisfies:

$$\|\tilde{x}(t)\| \leqslant \alpha = \max\left\{\sup_{-d\leqslant t\leqslant 0}\|\tilde{x}(t)\|, \eta^{-1}\tilde{\delta}\|R\|\right\} \quad (19)$$

And the fault $F(t)$ can be detected by a threshold criterion calculated from the norm of residual signal:

$$\|\varepsilon(t)\| > \beta := \alpha(\|\Gamma_1\| + \|\Gamma_2\|\|U_1\|\|E\|) + \tilde{\delta} \quad (20)$$

where α is determined by (18). When the norm of residual signal is larger than the threshold value β evaluated by Theorem 1, the fault can be detected.

5. Experimental results and discussion

To evaluate the proposed PDF estimation based detection model, a series of industrial experiments are carried out in a Chinese bauxite froth flotation plant. In the test runs, froth image videos are captured through the previously introduced monitoring system in the first rougher flotation cell. Subsequently, the froth videos are processed by the developed image analysis software which is capable of extracting bubble features on line. Fig. 6 presents the froth image segmentation results, which are collected and analyzed under the same condition in terms of resolution, angle, light condition, position, view scale, etc.

In practical flotation process experiments, the air flow rate and feed-in conditions are kept at a steady state so as to stabilize the production process. The addition of activator Na_2CO_3 becomes the major manipulating parameter, which directly determines pH value. As an indication of chemical addition, the bubble structures are one of determinants of mineral separation efficiency. Small bubbles with relative maximum surface area generally carry more valuable mineral particles, whose corresponding pH value is to be maintained to an acceptable bounded range. When one of the dominant operating variable chemical reagents is fluctuated, in this case the addition of Na_2Co_3, given that the collector KL and depressor 6P retain the regular amount, froth surface visual features such as bubble structure and color spectral information are reacting to the change of pH value. An increase in activator Na_2CO_3 addition was considered such that its simultaneous effect on bubble size distribution can be identified. As is shown in Fig. 6, the froth images evolved as the pH value increased gradually during a day, and the corresponding operational conditions were measured at the same time.

As for post-segmentation analysis, normal kernel with following basis functions is selected according to formula (7). The window width h is set to be 1.5 as a smoothing parameter, and centered points of each kernel $Z_i = 3.5i$, ($i = 1,\ldots,10$). Since the bubble radius involved ranges from 1 to 40 pixels (about 0–0.6 cm), the kernel functions with fixed window width are supposed to cover the entire radius range. Thus, the bubble size distribution can be

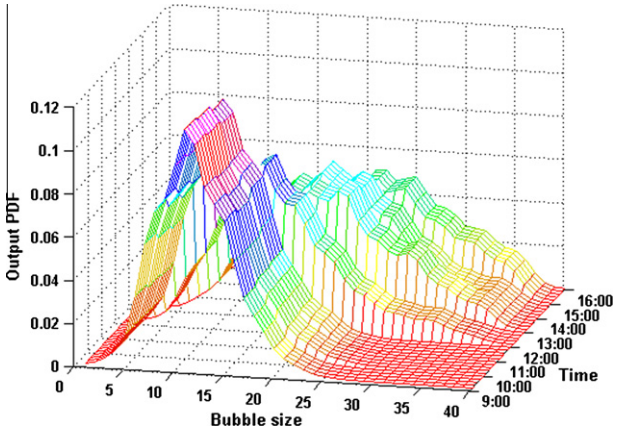

Fig. 7. The 3-D mesh plot of the output PDF. By applying the kernel estimation proposed in formula (7) to approximate the bubble size distributions of froth images in Fig. 6, the 3-D mesh plot of the output PDF when fault occurs is presented.

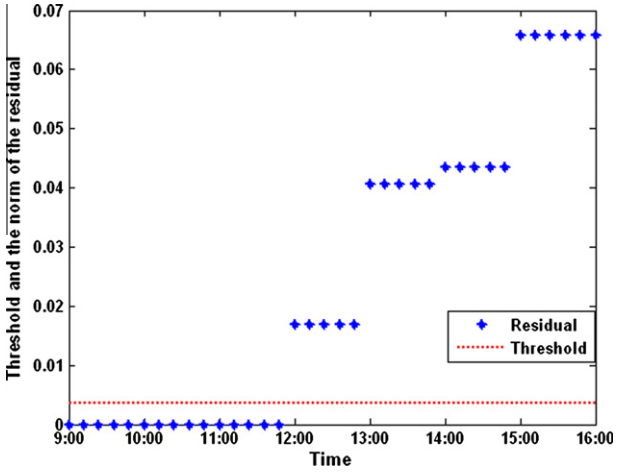

Fig. 8. The threshold and the responses of the norm of the residuals. The threshold with dotted line and the responses of the norm of the residuals froth images in Fig. 6 with asterisks are presented. It can be noted that the fault is successfully detected with the norm of residual over 0.0036.

approximated by (12), where $n = 10$. The weights $w_i(u,F)$ of normal kernel expansion have dimension of n, only $n - 1$ of which are independent. The approximation error $|\omega(z,u,F)| \leqslant \delta$, where $\delta \approx 0.001$.

By applying the kernel estimation on the bubble size distribution of froth images in Fig. 6, the 3-D mesh plot of the output PDF is shown in Fig. 7. At an hourly interval, the froth image video is captured at the point since it is reasonable to consider that the bubble size distribution is representative during a short time period in this study case. Meanwhile, the process operational conditions are measured on an hourly basis correspondingly. As can be seen, the bubble size distribution tends to shift dramatically when the addition of the activator Na_2CO_3 changed from 3293 g/t at 11:00 to 4129 g/t at 12:00, which resulted in pH value increased from 9.43 to 9.65 in response. And a continuous increase of pH values to 9.7 products a corresponding upward change of bubble size. Accordingly, the separation performance mineral recovery deteriorated from 73% at 11:00 to 50% at 15:00.

The fault detection filter model applied in this case is established as:

$$\begin{cases} \dot{x}(t) = Ax(t) + A_d x(t-d) + L\varepsilon(t) \\ \varepsilon(t) = \int_a^b \sigma(z)(f_{\ker}(z,u(t),F) - \hat{f}_{\ker}(z,u(t)))dz \\ W(t) = \hat{x}(t) \end{cases} \tag{21}$$

where $A = diag\{-0.83, -0.83, ..., -0.83\} \in R^{9\times 9}$, $A_d = diag\{0.2, 0.2, ..., 0.2\} \in R^{9\times 9}$.

Consider the delayed input as $u(t) = A_d x(t - d)$ where time delay $d = 2$. Since the error system converges to zero and stabilizes, -0.83 is given as the converging rate, and the coefficient A_d is the impacting factor of delayed input on present state. In formula (17), set $\sigma(z) = 1$, $|\Delta(t)| \leqslant 0.001 = \tilde{\delta}$. There exists a known matrix $U_1 = diag(1,1,...,1) \in R^{9\times 9}$ satisfies formula (15). To detect the fault, using LMI toolbox to solve the inequality of Theorem 1, $\lambda = 1$, $\eta = 0.176$, $\alpha = 0.00088$. According to $\beta = \alpha(\|\Gamma_1\| + \|\Gamma_2\|\|U_1\|\|E\|) + \tilde{\delta}$, threshold value can be calculated as $\beta = 0.0036$. Setting Fig. 6b as the standard PDF, Fig. 8 shows the threshold with dotted line and the responses of the norm of the residuals $\varepsilon(t)$ for froth images in Fig. 6 with asterisks. As can be seen, Fig. 6d–g are clearly identified as fault status because the residuals $\varepsilon(t) > \beta$ according to formula (20), which are consistent with the observation results from human operators.

Table 1
The detection performance of the testing database.

	Samples with correct detection	Samples with incorrect detection	Accuracy rate (%)
Fault status	26	1	96.3
Stable status	8	2	80
Total	34	3	91.89

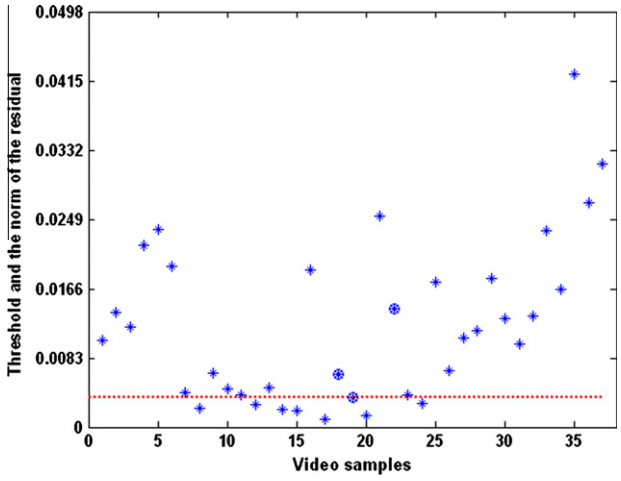

Fig. 9. The residuals of the testing froth video database. The dotted line represents the threshold for fault detection, and asterisks are the norms of the residual of each video sample. Three asterisks with outside circles are the samples with incorrect fault detection.

Attempts have been made in calculating false alarm rate on a testing database. The testing data consist of 37 offline froth videos captured from the bauxite flotation industry during April of 2010. The fault detection is accomplished by a threshold criterion calculated from the norm of residual signal in formula (20), according to which the residual signal above the threshold value indicates that a fault occurs. Table 1 gave the detection performance of the testing database. As can be seen in Fig. 9, dotted line represents the threshold for fault detection, and asterisks are the residual of each video sample. Three asterisks with outside circles are the samples with incorrect fault detection. The 19th sample should be categorized to the fault status, and the 18th and 22nd samples belong to the stable status in the system. The total fault detection accuracy on the database is 91.89%. It is possible that the false detection alarm ascribes to the segmentation malfunction of the captured froth images.

6. Conclusion

In this paper the description of bubble size probability density distribution and its inference to identify chemical operational status are investigated. After watershed segmentation analysis on froth images, the relationship between the film size distribution and the bubble size distribution is explored. Due to the poly dispersity of bubble distribution of the target froth images, the difference is not as remarkable as expected. Unlike tradition discussion of bubble structure focusing only on singular features including mean and variance insufficient to characterize the distribution profile. Nonparametric estimation based non-Gaussian stochastic variables are concerned. By using the normal kernel approximation, the fault detection problem is solved through a criterion determining the threshold of the norm of residual signal. Desired fault detection for reagent addition in froth flotation industry is achieved using the proposed method.

Appendix A

Proof of Theorem 1. Denote

$$\Pi_0 = \begin{bmatrix} \Pi_1 + \lambda^2 R\Gamma_2 R^T \Gamma_2^T & PA_d \\ A_d^T P & -I \end{bmatrix}$$

Using the Schur complement, $\Pi < 0 \Longleftrightarrow \Pi_0 + \eta I < 0$. Define the Lyapunov candidate as follows:

$$\begin{aligned} \dot{\Phi}(t) &= \Phi(t, \tilde{x}(t), x(t), \hat{x}(t)) \\ &= \tilde{x}^T(t)Px(t) + \int_{t-d}^{t} \tilde{x}^T(\tau)\tilde{x}(\tau)d\tau + \frac{1}{\lambda^2}\int_0^t [\|U_1 E\tilde{x}(\tau)\|^2 \\ &\quad - \|h(Ex(\tau)) - h(E\hat{x}(\tau))\|^2]d\tau \end{aligned}$$

Expand the derivation of this formula:

$$\begin{aligned} \dot{\Phi}(t) = \tilde{x}^T(t)P[&(A - L\Gamma_1)\tilde{x}(t) + A_d\tilde{x}(t-d) - L\Gamma_2(h(Ex(t)) - h(E\hat{x}(t))) \\ &- L\Delta(t)] + [\tilde{x}^T(t)(A - L\Gamma_1)^T + \tilde{x}^T(t-d)A_d^T - (h(Ex(t)) \\ &- h(E\hat{x}(t)))^T(L\Gamma_2)^T - (L\Delta(t))^T]P\tilde{x}(t) + \tilde{x}^T(t)\tilde{x}(t) - \tilde{x}^T(t-d)\tilde{x} \\ &\times (t-d) + \frac{1}{\lambda^2}[\|U_1 E\tilde{x}(t)\|^2 - \|h(Ex(t)) - h(E\hat{x}(t))\|^2] \end{aligned}$$

Combining of similar terms

$$\begin{aligned}\dot{\Phi}(t) &= 2\tilde{x}(t)(PA - R\Gamma_1)\tilde{x}(t) + 2\tilde{x}(t)PA_d\tilde{x}(t-d) - 2\tilde{x}(t)R\Gamma_2[h(Ex(t)) \\ &\quad - h(E\hat{x}(t))] - 2\tilde{x}(t)R\Delta(t) + \tilde{x}^T(t)x(t) - \tilde{x}^T(t-d)\tilde{x}(t-d) \\ &\quad + \frac{1}{\lambda^2}[\|U_1E\tilde{x}(t)\|^2 - \|h(Ex(t) - h(E\hat{x}(t)\|^2] = \tilde{x}^T(t)[(PA - R\Gamma_1) \\ &\quad + (PA - R\Gamma_1)^T + I]\tilde{x}(t) + \tilde{x}(t)PA_d\tilde{x}(t-d) + \tilde{x}(t-d)PA_d\tilde{x}(t) \\ &\quad - \tilde{x}^T(t-d)x(t-d) + \frac{1}{\lambda^2}\|U_1E\tilde{x}(t)\|^2 - \frac{1}{\lambda^2}(\|h(Ex(t)) - h(E\hat{x}(t))\|^2) \\ &\quad - 2\tilde{x}(t)R\Gamma_2[hE(x(t)) - h(E\hat{x}(t))] - 2\tilde{x}(t)R\Delta(t) \leqslant \tilde{x}^T(t)[(PA - R\Gamma_1) \\ &\quad + (PA - R\Gamma_1)^T + I]\tilde{x}(t) + \tilde{x}(t)PA_d\tilde{x}(t-d) + \tilde{x}(t-d)PA_d\tilde{x}(t) \\ &\quad - \tilde{x}^T(t-d)x(t-d) + \frac{1}{\lambda^2}\tilde{x}^T(t)E^TU_1^TU_1E\tilde{x}(t) + \lambda^2\tilde{x}^T(t)R\Gamma_2R^T\Gamma_2^T\tilde{x}(t) \\ &\quad - 2\tilde{x}(t)R\Delta(t) = \tilde{x}^T(t)[(PA - R\Gamma_1) + (PA - R\Gamma_1)^T + I + \frac{1}{\lambda^2}E^TU_1^TU_1E \\ &\quad + \lambda^2R\Gamma_2R^T\Gamma_2^T]\tilde{x}(t) + \tilde{x}(t)PA_d\tilde{x}(t-d) + \tilde{x}(t-d)PA_d\tilde{x}(t) \\ &\quad - \tilde{x}^T(t-d)x(t-d) - 2\tilde{x}(t)R\Delta(t) = \begin{pmatrix}\tilde{x}(t)\\ \tilde{x}(t-d)\end{pmatrix}^T \Pi_0 \begin{pmatrix}\tilde{x}(t)\\ \tilde{x}(t-d)\end{pmatrix} \\ &\quad - 2\tilde{x}(t)R\Delta(t)\end{aligned}$$

So

$$\dot{\Phi}(t) \leqslant \begin{pmatrix}\tilde{x}(t)\\ \tilde{x}(t-d)\end{pmatrix}^T \Pi_0 \begin{pmatrix}\tilde{x}(t)\\ \tilde{x}(t-d)\end{pmatrix} - 2\tilde{x}(t)R\Delta(t)$$

where $R = PL$. when $\|\tilde{x}(t)\| \leqslant \|\tilde{x}(t-d)\|$, $\phi(t) \leqslant -2\eta\|\tilde{x}(t)\|(\|\tilde{x}(t)\| - \eta^{-1}\tilde{\delta}\|R\|)$, which means that if $\|\tilde{x}(t)\| \leqslant \eta^{-1}\tilde{\delta}\|R\|$ then $\phi(t) \leqslant 0$. And similarly when $\|\tilde{x}(t)\| \geqslant \|\tilde{x}(t-d)\|$, $\phi(t) \leqslant -2\eta\|\tilde{x}(t)\|(\|\tilde{x}(t-d)\| - \eta^{-1}\tilde{\delta}\|R\|)$, so $\phi(t) \leqslant 0$ if $\|\tilde{x}(t-d)\| \geqslant \eta^{-1}\tilde{\delta}\|R\|$. Thus, when $\|\tilde{x}(t)\| \geqslant \eta^{-1}\tilde{\delta}\|R\|$, $\dot{\Phi} \leqslant 0$ holds, which means if $\|\tilde{x}(t)\| \leqslant \eta^{-1}\tilde{\delta}\|R\|$ occurs, $\dot{\Phi}$ start to be above zero, and the estimation error system is stable.

From the proof of Theorem 1, it can be seen that there exist a threshold of the fault to be the criterion of detecting the fault. Here we use the norm of the residual to calculate the fault.

$$\begin{aligned}\|\varepsilon(t)\| &\leqslant \|\Gamma_1\tilde{x}(t)\| + \|\Gamma_2\|\|h(Ex(t)) - h(E\hat{x}(t))\| + \|\Delta(t)\| \\ &\leqslant \|\Gamma_1\|\|\tilde{x}(t)\| + \|\Gamma_2\|\|U_1\|\|E\|\|\tilde{x}(t)\| + \|\Delta(t)\| \\ &\leqslant \alpha(\|\Gamma_1\| + \|\Gamma_2\|\|U_1\|\|E\|) + \delta = \beta\end{aligned}$$

when $\|\varepsilon(t)\| \geqslant \beta$, there happens a system fault. Then the proof is complete. □

References

Aldrich, C., Moolman, D.W., Bunkell, S.J., Harris, M.C., Theron, D.A., 1997. Relationship between surface froth features and process conditions in the batch flotation of a sulphide ore. Minerals Engineering 10 (11), 1207–1218.

Aldrich, C., Marais, C., Shean, B.J., Cilliers, J.J., 2010. Online monitoring and control of froth flotation systems with machine vision: a review. International Journal of Mineral Processing 96 (1–4), 1–13.

Bonifazi, G., Serranti, S., Volpe, F., Zuco, R., 2001. Characterisation of flotation froth colour and structure by machine vision. Computers and Geosciences 27 (9), 1111–1117.

Cilliers, J.J., Swartz, C.L.E., 1995. Simulation of quantitative fault diagnosis in backfill hydrocyclones. Minerals Engineering 8 (8), 871–882.

Guo, L., Wang, H., Wang, A.P., 2008. Optimal probability density function control for NARMAX stochastic systems. Automatica 44 (7), 1904–1911.

Himmelblau, D.M., 1978. Fault Diagnosis and Detection in Chemical and Petrochemical Processes. Elsevier Science, Amsterdam.

Holtham, P.N., Nguyen, K.K., 2002. On-line analysis of froth surface in coal and mineral flotation using JKFrothCam. International Journal of Mineral Processing 64 (2–3), 163–180.

Isermann, R., 1984. Process fault detection based on modelling and estimation methods – a survey. Automatica 20 (4), 387–404.

Liu, J.J., MacGregor, J.F., 2008. Froth-based modeling and control of flotation processes. Minerals Engineering 21 (9), 642–651.

Liu, J.J., Macgregor, J.F., Duchesene, C., Bartolacci, G., 2005. Flotation froth monitoring using multiresolutional multivariate image analysis. Minerals Engineering 18 (1), 65–76.

Monnereau, C., Vignes-Adler, M., 1998. Dynamics of 3D Real Foam Coarsening. Physical Review Letters 80 (23), 5228–5231.

Moolman, D.W., Aldrich, C., Schmitz, G.P.J., VanDeventer, J.S.J., 1996a. The interrelationship between surface froth characteristics and industrial flotation performance. Minerals Engineering 9 (8), 837–854.

Moolman, D.W., Eksteen, J.J., Aldrich, C., Deventer, J.S.J.V., 1996b. The significance of flotation froth appearance for machine vision control. International Journal of Mineral Processing 48 (3–4), 135–158.

Neethling, S.J., Cilliers, J.J., 2008. Predicting air recovery in flotation cells. Minerals Engineering 21 (12–14), 937–943.

Neethling, S.J., Lee, H.T., Cilliers, J.J., 2003. Simple relationships for predicting the recovery of liquid from flowing foams and froths. Minerals Engineering 16 (11), 1123–1130.

Niemi, A.J., Ylinen, R., Hyötyniemi, H., 1997. On characterization of pulp and froth in cells of flotation plant. International Journal of Mineral Processing 51 (1–4), 51–65.

O'Connor, C.T., Randall, E.W., Goodall, C.M., 1990. Measurement of the effects of physical and chemical variables on bubble size. International Journal of Mineral Processing 28 (1–2), 139–149.

Ross, V.E., 1991. An investigation of sub-processes in equilibrium froths (II): the effect of operating conditions. International Journal of Mineral Processing 31 (1–2), 51–71.

Sadr-Kazemi, N., Cilliers, J.J., 1997. An image processing algorithm for measurement of flotation froth bubble size and shape distributions. Minerals Engineering 10 (10), 1075–1083.

Scott, D.W., 1979. On optimal and data-based histograms. Biometrika 66 (3), 605–610.

Scott, D.W., 1985. Frequency polygons: theory and application. Journal of the American Statistical Association 80 (390), 348–354.

Wang, Y., Neethling, S.J., 2006. Simulating realistic froth surfaces. Minerals Engineering 19 (10), 1069–1076.

Wang, Y., Neethling, S.J., 2009. The relationship between the surface and internal structure of dry foam. Colloids and Surfaces A: Physicochemical and Engineering Aspects 339 (1–3), 73–81.

Wang, W., Wang, L., 2000. Froth image segmentation algorithms and their validation. In: International Conference on Signal Processing Beijing, pp. 2042–2045.

Wang, W., Bergholm, F., Yang, B., 2003. Froth delineation based on image classification. Minerals Engineering 16 (3), 1183–1192.

Yang, C., Xu, C., Gui, W., Du, J., 2009a. Nonparametric density estimation of bubble size distribution for monitoring mineral flotation process. In: 48th IEEE Conference on Decision and Control, Shanghai, pp. 2941-2945.

Yang, C., Xu, C., Mu, X., Zhou, K., 2009b. Bubble size estimation using interfacial morphological information for mineral flotation process monitoring. Transactions of Nonferrous Metals Society of China 19 (3), 694–699.

Zhang, Y.M., Guo, L., Wang, H., 2006. Filter-based fault detection and diagnosis using output PDFs for stochastic systems with time delays. Control Signal Process 20 (1), 175–194.